NOVEL SIMULATION TECHNIQUE EMPLOYED ON THE 1998 PAPUA NEW GUINEA TSUNAMI

P. WATTS
Applied Fluids Engineering
PMB #237, 5710 E. 7th Street, Long Beach, CA 90803

J. C. BORRERO
University of Southern California
Department of Civil Engineering, Los Angeles, CA 90089

D. R. TAPPIN
British Geological Survey
Keyworth, Nottingham, NG12 5GG, United Kingdom

J.-P. BARDET
University of Southern California
Department of Civil Engineering, Los Angeles, CA 90089

S. T. GRILLI
University of Rhode Island
Department of Ocean Engineering, Narragansett, RI 02882

C. E. SYNOLAKIS
University of Southern California
Department of Civil Engineering, Los Angeles, CA 90089

Abstract. Researchers have postulated that the 1998 Papua New Guinea (PNG) tsunami may have been generated by a submarine mass movement. Indeed a candidate event has been located during marine surveys. Attempts to simulate the tsunami with new bathymetric data have generally been able to reproduce the observed longshore distribution of runup but not the measured tsunami amplitude. A novel simulation technique reproduces all gross features of the PNG tsunami by: 1) considering the local geology and soil mechanics, 2) estimating the slump dimensions, 3) calculating the center of mass motion, 4) simulating tsunami generation with full fluid dynamic field equations, and 5) propagating tsunami waves with a depth averaged code. Preliminary simulations showed that slump deformation is 10-40 times less important than slump center of mass motion for such an event. The soil mechanics of slump failure informed an analysis of slump center of mass motion specific to this event. The marine geology is

an essential component of our work. This simulation technique sets a new standard with which to evaluate simulations of tsunamis generated by submarine mass failure.

1. Introduction

On July 17, 1998, a tsunami struck Aitape, Sundaun Province, Papua New Guinea (PNG) about twenty minutes after a nearby magnitude 7 earthquake. Shortly after 7 PM local time, more than 25 km of the northern PNG coastline home to at least 10,000 people was swept clean by water approximately 10 meters high. More than 2200 people perished during the tsunami or shortly thereafter. The peak measured water height of 15 meters above sea level was 3-30 times larger than expected and constitutes the largest documented tsunami related to a magnitude 7 earthquake in the 1990s. The scale of the tragedy, the unexpectedly large tsunami amplitude, and the complex regional geology have motivated an international effort to understand tsunami generation. Goals include assessing future tsunami hazards for the area, testing tsunami simulation and inundation computations, and developing tsunami education for coastal communities facing similar hazards.

Two weeks after the event, an International Tsunami Survey Team (ITST) began documenting the maximum waterline, or runup, and found water marks up to 15 meters above sea level (Kawata *et al*., 1999). The narrow distribution of the maximum runup along the coastline indicated local tsunami generation directly off Sissano Lagoon (Kawata *et al*., 1999; Davies, 1998). The unusually large peak runup relative to the earthquake magnitude led the ITST to hypothesize tsunami generation by a giant submarine mass failure, a broad geological term that includes submerged reef failure, underwater slides, and underwater slumps (Schwab et al., 1993). Eyewitness accounts from Malol (Figure 1) describe the tsunami arriving just after a strong aftershock, or about 21 minutes after the main shock (Kawata *et al*., 1999; Davies, 1998). An apparent delay of about ten minutes between the main shock and tsunami generation provides strong evidence of mass failure tsunami generation. Submarine masses may be expected to fail minutes after strong ground motion ceases (Bjerrum, 1971; Housner, 1985; Murty, 1979; Turner and Schuster, 1996) and to generate tsunami features, such a leading depression N-wave similar to those observed in PNG (Watts, 1998; Watts, 2000). Delays in mass failure may be attributed to complex nucleation of a failure plane in metastable sediment, or to a secondary trigger such as an aftershock or an increase in water pressure.

2. Tsunami Sources

An alternative source mechanism of the PNG tsunami is coseismic displacement of the sea floor resulting from earthquake rupture. These permanent sea floor displacements often generate tsunamis with longer wavelengths, longer periods, and a larger source area than those generated by mass failures (Watts, 1998; Watts, 2000; Hammack, 1973).

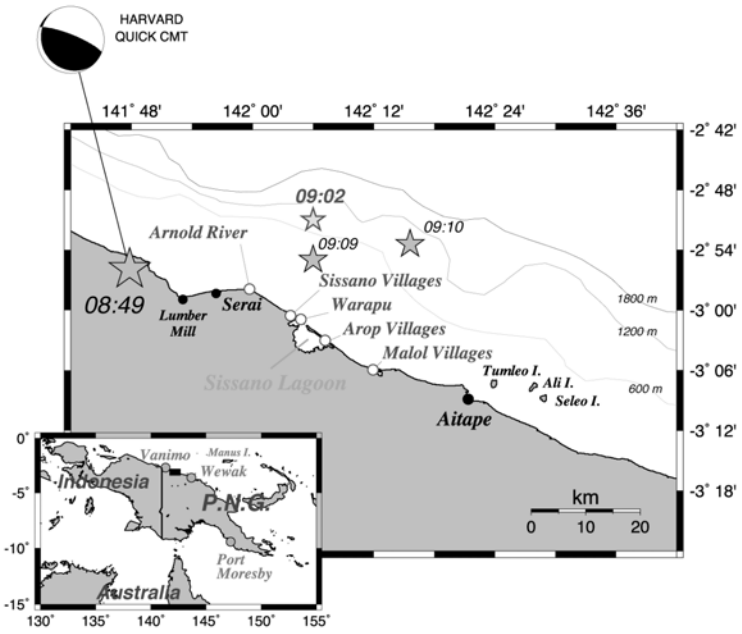

Figure 1. Map of the affected region indicating village sites and seismic events.

Hence, coseismic displacement can produce transoceanic tsunamis, whereas mass failures produce tsunamis that decay rapidly away from the generation region (Davies, 1998; Plafker *et al*., 1969), except along the axis of failure (Iwasaki, 1997). Coseismic displacement generates tsunami amplitudes that correlate with earthquake magnitude (Hammack, 1973; Geist, 1998); submarine mass failures produce tsunamis with amplitudes limited only by the vertical extent of center of mass motion (Murty, 1979; Watts, 1998). Both mass failure center of mass motion and the subsequent tsunami amplitude can surpass those of coseismic displacement by two orders of magnitude (Schwab et al., 1993; Watts, 1998), posing a greater threat to coastal communities than previously recognized.

Historical records verify the tsunami hazard posed by submarine mass failure. Most tsunami damage and fatalities within Prince William Sound following the 1964 Good Friday, Alaskan earthquake resulted from local waves generated by submarine mass failure (Plafker *et al*., 1969). Tsunamis generated by mass failure were larger in amplitude and arrived earlier than the transoceanic tsunami attributed to the earthquake. Since 1992, there have been eleven major local tsunamis: Nicaragua, 1992; Flores

Island, Indonesia, 1992; Okushiri, Japan, 1993; East Java, Indonesia, 1994; Shikotan, South Kuril Islands, 1994; Mindoro, Philippines, 1994; Skagway, Alaska, 1994; Irian Jaya, Indonesia, 1996; Chimbote, Peru, 1996; Kamchatka, Russia, 1997; Aitape, Papua New Guinea, 1998. The majority of these tsunamis demonstrated regions of peaked longshore runup distributions. For example, runup produced during the Flores Island tsunami showed a modest plateau of 2-8 m corresponding to the earthquake moment magnitude that was punctuated by numerous large peaks up to 26 m high that correlate with reef failure and subaerial landslides (Imamura and Gica, 1996). Four other events – Nicaragua, Mindoro, Skagway, and Kamchatka – are known or suspected to have involved significant mass failure tsunami generation, with or without significant coseismic displacement. Tsunamigenic submarine mass failures appear to be involved in many of the largest tsunamis this decade, and in at least several instances to be the very cause of peak runup. Unfortunately, tsunami catalogues do not yet distinguish between the source of mean runup and the source of peak runup.

3. Marine Surveys

Several months after the PNG tsunami, marine surveys were carried out on the R/V *Kairei* (KR98-13) and R/V *Natsushima* (NT99-02) joint Japan Marine Science and Technology Center (JAMSTEC) and South Pacific Applied Geoscience Commission (SOPAC) cruises. Bathymetric data were collected on the *Kairei* by a Sea Beam 2112 multibeam survey system capable of wide swath mapping and side scan imaging using multiple 12 kHz acoustic beams. The bathymetry revealed a large arcuate amphitheater near 2.89˚S and 142.26˚E as well as an uplifted block around 2.80˚S and 142.22˚E (Figure 1). Remotely operated vehicle (ROV) observations made on the *Natsushima* revealed evidence of strong ground motion from the amphitheater to the uplifted block. The presence of fresh headwalls, breccia blocks, scree slopes, tension cracks, and basement faulting between these geological features defined the tsunami source region. A fresh slump at the foot of the amphitheater was identified as the probable cause of the tsunami (Tappin *et al*., 1999). This particular mass failure is termed an underwater slump on account of deep rotational failure in stiff clay. Onboard simulations performed with the new bathymetry data revealed that wave refraction by two submarine canyons focused tsunami energy towards Sissano Lagoon, but computed tsunami amplitudes remained two times less than measured runup values (Tappin *et al*., 1999). Two ROV dives revealed little evidence of ground motion more than 30 km from the PNG shoreline, and the remaining ROV dives revealed only decimeters of vertical fault displacement around the amphitheater (Tappin *et al*., 2001).

4. Seismic Records

The main shock took place at 08:49 GMT and had an epicenter near 2.961˚S and 141.926˚E with rupture probably extending eastwards towards the tsunami source region

(Figures 1). According to a recently devised energy-to-moment test (Newman and Okal, 1998); Wyesession *et al*., 1991), this shock did not undergo unusually slow rupture, a characteristic known to enhance tsunami generation. The US Geological Survey (USGS) documents one m_b=4.4 seismic event at 09:02 and a smaller one at 09:06 (Figure 2). A widely felt aftershock was composed of one shock due north of Sissano Lagoon at 09:09 followed 31 seconds later by a second shock ~15 km further east (Figures 1). Eyewitness accounts at Malol indicate tsunami arrival immediately after these aftershocks (Kawata *et al*., 1999; Davies, 1998; Tappin *et al*., 1999). Villagers on the sandy spit in front of Sissano Lagoon did not notice these aftershocks, probably because ground motion was filtered by ubiquitous sediment liquefaction. Evidence for liquefaction beneath the sandy spit includes sand boils, water spouts, and apparent settlement. Moreover, the probable rupture direction was towards Tumileo Island, where the main shock and widely felt aftershocks produced comparable ground motion. The perceived ground motion depends on both location and sediment.

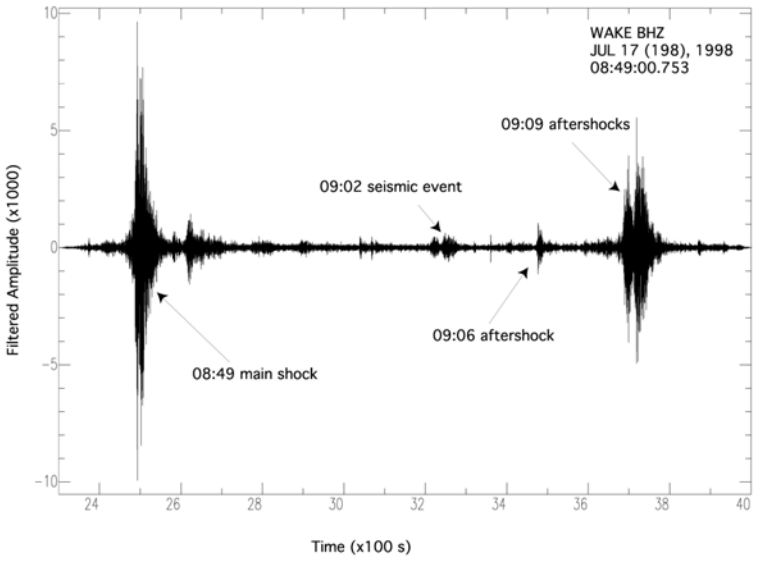

Figure 2. Record of PNG seismic events at Wake Island from T Phases.

The aftershock distribution supports a shallow dipping failure mechanism as well as our location of the main shock. The aftershock epicenters surround the tsunami source region with an area of about 40 km by 70 km. This suggests that the shallow dipping fault mechanism is a more likely description of the main shock than the steeply dipping

fault mechanism (Kawata *et al*., 1999; Davies, 1998; Tappin *et al*., 2001). The main shock appears to arise from rupture along the subducting Pacific Plate at an initial depth of around 5-15 km. Rupture may have propagated eastward from a hypocenter near the western edge of the aftershock area. Steeply dipping faults can be expected for backarc and outer rise earthquakes (Tappin *et al*., 1999). However, a tsunami generated by coseismic displacement on the margin would arrive ten minutes too early. Tsunami generation by coseismic displacement beyond the New Guinea Trench would require an epicenter 180 km from the PNG shoreline to reproduce tsunami arrival times. This is well beyond published epicenter locations and outside of the apparent tsunami source region. Tsunami propagation times are controlled exclusively by water depth, with deeper water allowing the waves to travel faster.

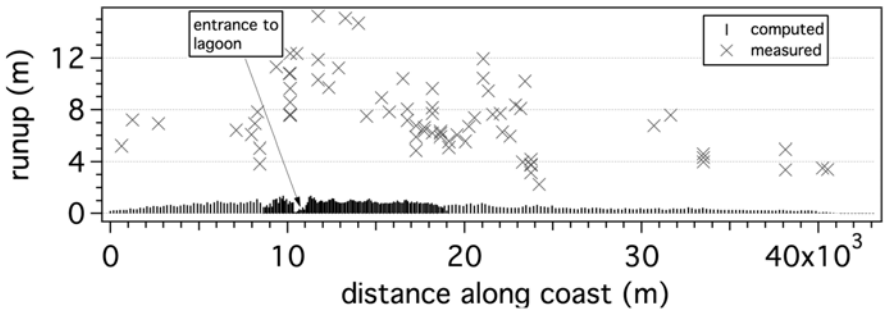

Figure 3. Maximum tsunami runup due to the main shock compared with measurements.

We simulated tsunami generation by the main shock in order to evaluate tsunami amplitude and arrival times related to coseismic displacement. The shallow dipping normal fault mechanism has a strike of 146º, dip of 19º, and rake of 127º (Kawata *et al*., 1999). We considered a seismic moment of 5.2×10^{19} N-m and a rigidity of 30 GPa when calculating ground deformation. Characteristic slip along the rupture plane is about 2 meters. We modeled rupture extending eastward from the hypocenter, nearly parallel with the shoreline and directed towards the tsunami source region. By transposing vertical sea floor displacement instantaneously to the free surface, we arrive at an initial tsunami amplitude of up to 40 cm. This displacement corresponds to vertical offsets observed along basement faults during ROV dives in the source region. Our simulations reproduce peak runup less than one meter along the affected shoreline 7-8 minutes following the main shock (Figure 3). These waves could easily pass unnoticed in the surf zone. Since far-field tsunami amplitudes depend primarily on moment magnitude, we know that our shallow dipping fault simulation can reproduce observations of a 20 cm tsunami near Japan. In other words, we only invoke the underwater slump in order to explain the timing and amplitude of the local tsunami.

Based on our understanding of tsunami propagation and arrival times, tsunami generation most likely corresponds to the 09:02 seismic event if it corresponds to any at all. Even to the naked eye, this seismic event appears to have a parabolic amplitude envelope mimicking acceleration and deceleration of a slump more than the sharp decay of an aftershock (Figure 2). We postulate that this mild seismic event records slump failure, perhaps initiated by high pressure water advecting up a control fault from the subduction zone. The 09:02 seismic event has an epicenter at 2.85˚S and 142.26˚E with an elliptical confidence margin that includes the slump (Figure 1). For comparison, the 100 times more massive 1929 Grand Banks and 1975 Kalapana submarine mass failures produced readily detected seismic records (Hasegawa and Kanamori, 1987; Eissler and Kanamori, 1987). Mild failure plane inclination, low sediment density, low sediment stiffness and water buoyancy tend to make underwater mass failures difficult to detect relative to subaerial events or earthquakes (Seed *et al*., 1988). The PNG slump generated an order of magnitude less seismic energy than the Mount St. Helens subaerial landslide (with mantle magnitude $M_m \approx 5.4$) despite similar volumes (Kanamori *et al*., 1984). Regardless, we can expect detectable seismic radiation from an underwater slump of this size (see below).

5. Numerical Models

Modeling tsunami generation by submarine mass failure remains a formidable undertaking. Jiang and Leblond (1992) developed depth-averaged wave equations by representing submarine mass failures as volumes of immiscible fluid. Benefits of this approach include analytical simplicity and mass failure deformation. However, because horizontal fluid accelerations are known to be present during submarine mass failure, Grilli and Watts (1999) and Heinrich (1992) model the complete fluid dynamics of tsunami generation. Cohesive slump motion along a circular arc differs significantly from that of noncohesive slides along a straight plane (Watts, 1998; Grilli and Watts, 1999), accounting for the inability of earlier PNG slide simulations to describe tsunami generation for this event. Hence, the earlier models that focused on deformation (e.g., Jiang and LeBlond, 1992) are not necessarily relevant to this event because they reproduce only slide motions. Sliding typically involves rectilinear failure of deformable silt or sand on top of a low friction lubricating layer; slumping often involves deep failure of stiff clay with residual shear strength restraining motion (Schwab *et al*., 1993; Turner and Schuster, 1996; Prior and Coleman, 1979). With these distinct center of mass motions, we find that tsunami amplitudes and periods can differ by factors of 2-5 for failure of cohesionless versus cohesive sediments of identical shape and density (Figure 4). In contrast, a reasonable underwater landslide rate of deformation changes tsunami amplitude by less than 10% and has no significant effect on wavelength (Figure 5). Clearly, tsunami generation by submarine mass failure requires foremost an accurate center of mass motion.

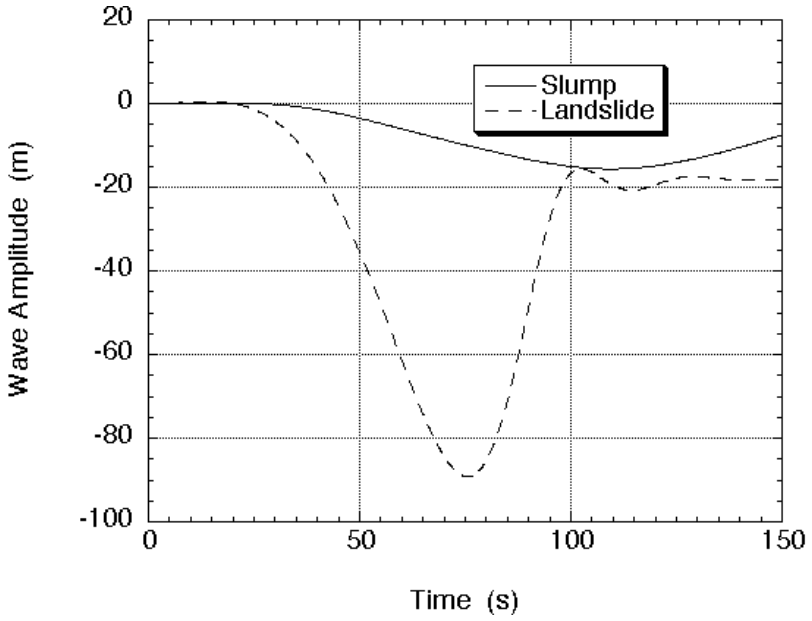

Figure 4. Comparison of tsunami generation by an underwater slide and slump.

6. PNG Simulation

We develop and demonstrate a novel tsunami simulation technique that overcomes these deficiencies. First, we note that geological evidence indicates a cohesive slump. A push core taken by the ROV along the exposed failure plane revealed stiff biogenic mud. Second, we determined mass failure geometry. Sub-bottom profiles and seismic records revealed internal failure planes that lacked significant relative motion. Hence, the main mass of cohesive sediment moved as a deformable block and we choose to employ a maximum initial slump thickness of T=600 meters. Careful inspection of the bathymetry and seismic data combined with ROV observations indicate a slump w=4 km wide and b=4.5 km long. These dimensions are consistent with documented thickness to length ratios of 5-15% for deep failure of cohesive marine sediments (Schwab et al., 1993; Edgers and Karlrud, 1982). Assuming parabolic profiles across both width and length, this slump involved about 4 cubic km of sediment, modest by

geological records that sometimes exceed 1000 cubic km (Schwab *et al*., 1993; Turner and Schuster, 1996; Prior and Coleman, 1979).

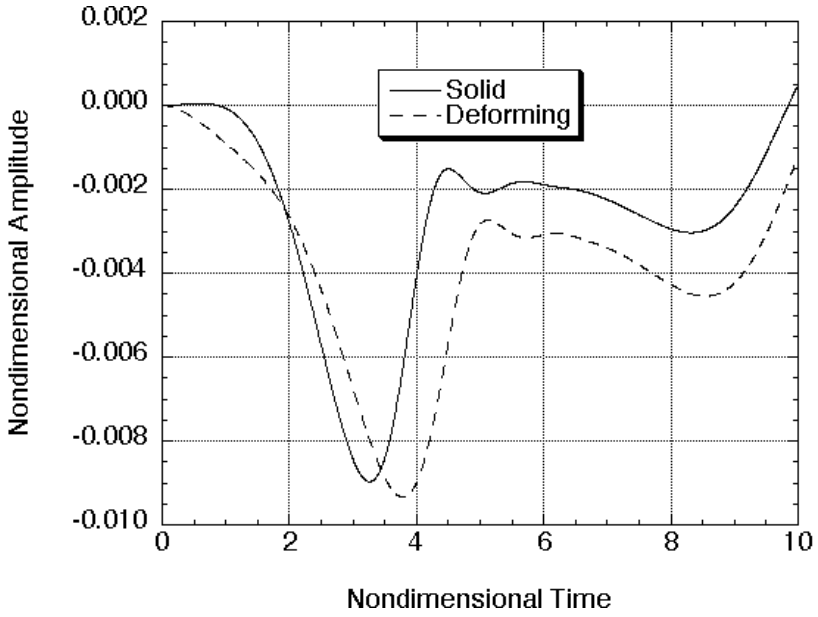

Figure 5. Impact on tsunami generation of maximum expected rate of deformation.

Third, since the center of mass motion is essentially decoupled from wave generation (Watts, 2000; Jiang and LeBlond, 1992), we solve equations of motion tailored to the local geology. We therefore model the PNG slump as a rigid body rotating along a circular arc subject to external moments from added mass, buoyancy, gravity, and a constant residual shear stress (Kanamori et al., 1984; Bardet, 1997; Batchelor, 1967). We neglect slump deformation because it is a secondary effect for tsunami generation (Figure 5). We solve the linear differential equation of a damped pendulum

$$R\,(m_b + C_m\,m_o)\,\frac{d^2\phi}{dt^2} = (m_b - m_o)\,g\,\phi \;-\; w\,b\,S_u \qquad (1)$$

by invoking the small angle approximation for the angular displacement ϕ. The post-failure sediment shear strength S_u retards slump motion at all times. We assume an added mass coefficient C_m=1 (Schwab *et al*., 1993; Batchelor, 1967). Multiplying the solution of (1) by the radius of curvature R≈7 km (Figure 6) gives the slump center of mass displacement along the failure arc

$$s(t) = s_o \left[1 - \cos\left(\frac{t}{t_o}\right)\right] \tag{2}$$

as a function of time subject to s(0)=0 and $0<t/t_0<\pi$. The characteristic distance and characteristic time of slump motion are found from equations (1) and (2) to be

$$s_o = \frac{R(\phi_f - \phi_i)}{2}, \quad t_o = \sqrt{\frac{R(\gamma + C_m)}{g(\gamma - 1)}}. \tag{3}$$

Based on the initial angle ϕ_i=-0.351 radians and final angle ϕ_f =-0.065 radians of the center of mass (Figure 6) and a slump specific density γ=2.14, we calculate an initial acceleration $a_0=s_0/t_0^2\approx0.51$ m/s^2 and maximum velocity $u_{max}=s_0/t_0\approx23$ m/s which differ by less than 3% with the exact solution of the nonlinear differential equation, including fluid dynamic drag (Nayfeh and Mook, 1979). Our simulation technique provides the reasonable initial acceleration needed to model tsunami generation (Watts, 1998; Watts, 2000).

Fourth, we incorporate the center of mass motion into a complete fluid dynamic simulation of tsunami generation, employing the 2D boundary element model of Grilli and Watts (1999) to solve inviscid, irrotational equations of fluid motion. The slump was approximated by a b=4.5 km long and T=600 meter thick semi-ellipse that translated about $s_0\approx1.0$ km along the failure plane with the slump center of mass motion given by (2). Tsunami amplitude consistently grew during the first t_0=44 seconds of slump acceleration and ceased to grow thereafter as waves propagated both towards shore and out to sea (Figure 7). The origin of this profile is at the shoreline. Around the time $t=t_0$, most of the tsunami energy is invested in wave potential energy, as opposed to wave kinetic energy (Watts, 2000). Therefore, we curve fit the wave profile at $t=t_0$ with two Gaussians, one for the depression wave and one for the elevation wave. Tsunami amplitudes from these simulations are proportional to the slump thickness and proportional to the length to depth ratio raised to the 1.25 power, enabling analytical sensitivity analyses.

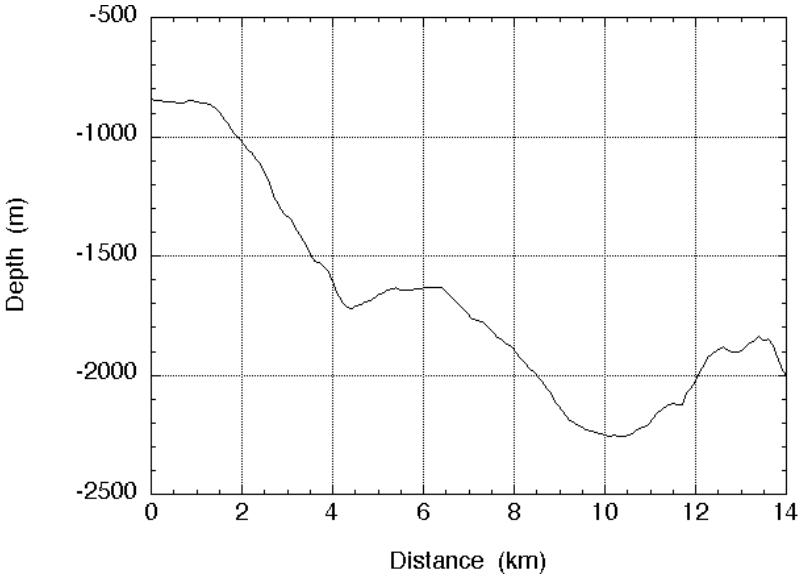

Figure 6. Transect of the underwater slump beginning at 2.92˚S and 142.25˚E.

The w=4 km wide slump generated water waves in a depth of d≈1 km, suggestive of essentially 2D wave generation. We accounted for 3D effects by assuming a parabolic transverse wave profile of width w in the absence of transverse wave propagation. For the duration t_0 of tsunami generation, the width of the wave will increase to approximately (w+λ) and take on a form not dissimilar to

$$\frac{w}{w+\lambda}\,\mathrm{sech}^2\,\frac{3(y-y_o)}{w+\lambda} \tag{4}$$

where w is the slump width, $\lambda=t_0\sqrt{gd}$ =4.4 km is the tsunami wavelength, and y is measured perpendicular to the transect. The factor of three is chosen to yield a relative wave amplitude of 1% at the transverse distance $y-y_0=w+\lambda$. Conservation of mass dictates a reduction of w/(w+λ)≈0.5 in the overall tsunami amplitude due to transverse propagation.

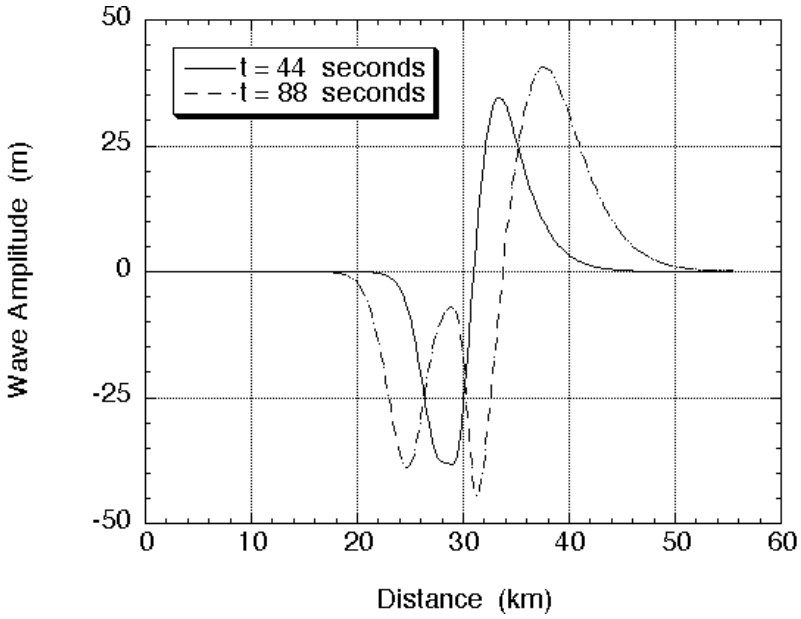

Figure 7. Profile of tsunami amplitude along transect at 44 and 88 seconds after slump failure.

Finally, we input the 3D tsunami shape at t_0=44 seconds into an accurate tsunami propagation and runup model

$$\eta(x,y) = \mathrm{sech}^2\left(\frac{3\,(y - y_O)}{8.4}\right)\,\left(-35.71\,\exp\left(-0.10128\,(x - 29.066 - x_O)\right)^2 + \right.$$

$$\left. + 25.14\,\exp\left(-0.051693\,(x - 31.709 - x_O)\right)^2\right) \qquad (5)$$

where x_0 and y_0 position the tsunami shape above the slump. Titov and Synolakis (1998) solve the nonlinear shallow water wave equations as a system of hyperbolic differential equations able to simulate overland flow by extending the simulation domain. We neglected water velocities when transferring the tsunami profile to this model. Such refinement awaits a numerical interface that will link these two models. The *Kairei* cruise effectively mapped depths greater than 400 meters. Depths from the shoreline out to 150 meters were interpolated from the Aus. 389 chart. We merged

depths between 150-400 meters by linear interpolation to complete the bathymetry. Onland transects made by the ITST provided topography around Sissano Lagoon (Kawata *et al*., 1999). Wave interactions with a coastline are most affected by the shallowest regions and consequently all PNG simulations remain qualitative (Kangolu and Synolakis, 1998). For this reason, we employed a grid spacing of 200 meters.

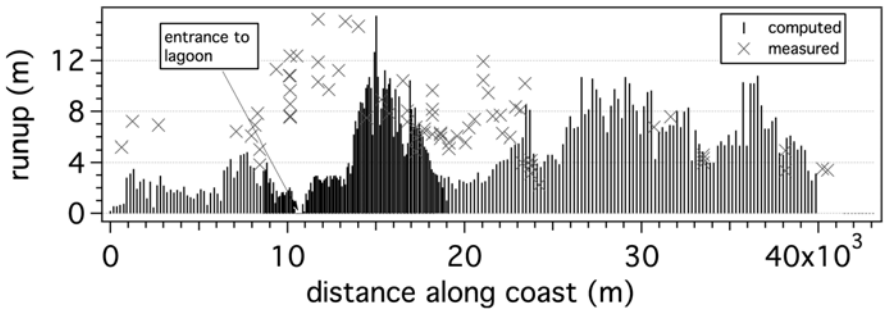

Figure 8. Maximum tsunami runup due to the slump compared with measurements.

Our maximum runup results, based on the combined mass failure geology, geometry and motion analyses linked with generation and propagation models, compare favorably with field runup measurements (Figure 8). Agreement between simulated and measured longshore distribution of runup is governed primarily by bathymetry and would improve with more accurate nearshore bathymetry, as shown by Tappin *et al*. (2001). Tsunami arrival times based on simulation results are 09:10 at Malol and 09:11 at Arop and Sissano. Eyewitness accounts from Malol describe tsunami arrival as soon as ground motion from the widely felt aftershocks at 09:09 ceased (Davies, 1998). The tsunami first attacked Malol, then Sissano soon afterwards, both because of deep submarine canyons. All simulations of tsunami generation within the source region predict first tsunami attack at Malol based on existing bathymetry. Tsunami arrival converged from both east and west on the sandy spit in front of Sissano Lagoon, also in agreement with eyewitness accounts and physical evidence (Kawata et al., 1999; Davies, 1998). Our analyses of tsunami amplitude and timing support tsunami generation by a giant underwater slump.

7. Geotechnical Analysis

With hindsight, geotechnical analysis would have indicated that slump failure is a distinct possibility for earthquakes in this region. We estimated a mean shear stress of 0.5 MPa and a mean effective overburden of 4.4 MPa along the initial failure plane. From these values, we calculated an average residual undrained shear strength along the initial failure plane for normally consolidated sediment S_u~0.5-1.5 MPa that is within

the range of accepted values measured for other stiff clays (Bardet, 1997). We expect a sediment-starved and subsiding margin to have normally consolidated sediments (Tappin *et al*., 1999; Bardet, 1997). The largest peak horizontal acceleration required for an earthquake to induce static failure is 0.5 g, which is an acceptable value for a moment magnitude M_W>6.5 earthquake within a 10 km radius of the epicenter (Joyner and Boore, 1981). The slump was in line with seismic energy release and therefore subject to strong ground motion as demonstrated by ROV investigation of the tsunami source region. The delay in failure suggests that ground motion did not shake the slump loose. A water pressure of less than 1 MPa injected near the base of the slump is sufficient to induce failure.

8. Conclusions

The PNG event shows that submarine mass failures can generate large tsunamis that strike nearby coastlines shortly after a moderate earthquake. Uncertainty in tsunami amplitude and arrival time when generated by nearby mass failures further complicates tsunami hazard assessment and warning. We expect tsunamigenic mass failure for earthquakes with moment magnitudes as low as M_W≈5. Hence, coastal populations may not be aware of potential tsunami generation. The best protection from tsunami hazards is to stay away from vulnerable sections of coastline. Nevertheless, the PNG tsunami is a case study with which to educate established coastal populations: to be foremost aware of the imminent dangers following a receding sea, and second of all to seek safe elevations following any felt earthquake. Our combined generation and propagation models are part of a new and accurate technique to assess tsunami hazards from submarine mass failures. For well-studied margins, our geotechnical analysis indicates that the occurrence of submarine mass failures can be predicted for a given earthquake from fundamental geological and geotechnical information. Hence, we may be able to predict coastal areas vulnerable to tsunami attack due to mass failure.

9. Acknowledgments

Tappin and Watts acknowledge SOPAC, JAMSTEC and PNG for organizing two research cruises on short notice. Watts is grateful for support from NSF to report cruise findings to SOPAC and from FEMA to attend the IUGG meeting. Borrero and Synolakis received support from NSF for a field survey in PNG two weeks after the event. Prof. Emile Okal from Northwestern University provided material for the figures and calculated the vertical coseismic displacement from the main shock. Mr. Koshimura from Tohoku University kindly provided digitized nearshore bathymetry data. Prof. McMurtry from the University of Hawaii provided sediment density from *Kairei* piston cores.

10. References

Bardet, J.-P., 1997: *Experimental soil mechanics,* Prentice Hall, Upper Saddle River, NJ.
Batchelor, G. K., 1967: *An Introduction to Fluid Dynamics*, Cambridge University Press, Cambridge, UK.
Bjerrum, L., 1971: Subaqueous slope failures in Norwegian fjords, *Nor. Geotech. Inst. Bull.*, **88**, 1-8.
Davies, H., 1998: *The Sissano Tsunami*. Published by the author, Port Moresby, PNG.
Edgers, L., and K. Karlsrud, 1982: Soil flows generated by submarine slides: case studies and consequences, *Nor. Geotech. Inst. Bull.*, **143**, 1-11.
Eissler, H. K., and H. Kanamori, 1987: A single-force model for the 1975 Kalapana, Hawaii, earthquake, *J. Geophys. Res*., **92**(B6), 4827-4836.
Geist, E. L., 1998: Local tsunamis and earthquake source parameters, *Adv. in Geophys.*, **39**, 117-209.
Grilli, S. T., and P. Watts, 1999: Modeling of waves generated by a moving submerged body: Applications to underwater landslides, *Engrg. Analysis with Boundary Elements*, **23**(8), 645-656.
Hammack, J. L., 1973: A note on tsunamis: Their generation and propagation in an ocean of uniform depth, *J. Fluid Mech.*, **60**, 769-799.
Hasegawa, H. S., and H. Kanamori, 1987: Source mechanism of the magnitude 7.2 Grand Banks earthquake of November 1929: Double couple or submarine landslide?, B*ull. Seis. Soc. Am*., **77**(6), 1984-2004.
Heinrich, P., 1992: Nonlinear water waves generated by submarine and aerial landslides, *J. Wtrwy, Port, Coast, and Oc. Engrg.*, ASCE, **118**(3), 249-266.
Housner, G. W., 1985: *Liquefaction of soils during earthquakes,* National Academy Press, Washington, D.C.
Imamura, F., and E. C. Gica,, 1996: Numerical model for tsunami generation due to subaqueous landslide along a coast, *Sci. Tsunami Hazards*, **14**, 13-28.
Iwasaki, S., 1997: The wave forms and directivity of a tsunami generated by an earthquake and a landslide, *Sci. Tsunami Hazards*, **15**, 23-40.
Jiang, L., and P. H. LeBlond, 1992: The coupling of a submarine slide and the surface waves which it generates, *J. Geoph. Res.*, **97**(C8), 12731-12744.
Joyner, W. B., and D. M. Boore, 1981: Peak horizontal acceleration and velocity from strong-motion records including records from the 1979 Imperial Valley, California earthquake, *Bull. Seis. Soc. Am.*, **71**(6), 2011-2038.
Kanamori, H., J. W. Given, and T. Lay, 1984: Analysis of seismic body waves excited by the Mount St. Helens eruption of May 18, 1980, *J. Geophys. Res*., **89**, 1856-1866.
Kanoglu, U., and C. E. Synolakis, 1998: Long wave runup on piecewise linear topographies, *J. Fluid Mech*., **374**, 1-28.
Kawata, Y. and International Tsunami Survey Team members, 1999: Tsunami in Papua New guinea was intense as first thought, *Eos, Trans. Am. Geophys. Union*, **80**(9), 101.
Murty, T. S., 1979: Submarine slide-generated water waves in Kitimat inlet, British Columbia, *J. Geoph. Res.*, **84**(C12), 7777-7779.
Nayfeh, A. H., and D. T. Mook, 1979: *Nonlinear Oscillations,* Wiley-Interscience, New York, NY.
Newman, A. V., and E. A. Okal, 1998: Teleseismic estimates of radiated seismic energy: The E/ M0 discriminant for tsunami earthquakes, *J. Geophys. Res*., **103**, 26885-26898.
Plafker, G., R. Kachadoorian, E. B. Eckel, and L. R. Mayo, 1969: *The Alaska earthquake March 27, 1964: Various communities*, U.S. Geol. Surv. Prof. Paper 542-G, U.S., Dept. of Interior, Washington, D.C.
Prior, D. B., and J. M. Coleman, 1979: Submarine landslides: Geometry and nomenclature, *Z. Geomorph. N. F.*, **23**(4), 415-426.
Schwab, W. C., H. J. Lee, and D. C. Twichell, 1993:. *Submarine landslides: Selected studies in the U.S. exclusive economic zone,* U.S. Geol. Surv. Bull. 2002, U.S., Dept. of Interior, Washington, D.C.
Seed, H. B., R. B. Seed, F. Schlosser, F. Blondeau,, and I. Juran, 1988: The landslide at the Port of Nice on October 16, 1979, *Rep. No. UCB/EERC-88/10*, Earthquake Engineering Research Center, University of California, Berkeley, CA.
Tappin, D. R., T. Matsumoto, and shipboard scientists, 1999: Offshore geological investigation of the July 1998 Sissano tsunami, Papua new Guinea, *EOS, Trans. Am. Geophys. Union*, **80**(30), 329.
Tappin, D. R., P. Watts, G. M. McMurtry, Y. Lafoy, and T. Matsumoto, 2001: The Sissano, Papua New Guinea tsunami of July 1998 – offshore evidence on the source mechanism, *Marine Geology*, **175**, 1-23.
Titov, V. V., and C. E. Synolakis, 1998: Numerical modeling of tidal wave runup, *J. Wtrwy., Port, Coast., and Oc. Engrg.*, ASCE, **124**(4), 157-171.
Turner, A. K., and R. L. Schuster, 1996: *Landslides: Investigation and mitigation,* Special Report 247, Trans. Res. Board, National Academy Press, Washington, D.C.

Watts, P., 1998: Wavemaker curves for tsunamis generated by underwater landslides, *J. Wtrwy, Port, Coast, and Oc. Engrg.*, ASCE, **124**(3), 127-137.

Watts, P., 2000: Tsunami features of solid block underwater landslides, *J. Wtrwy, Port, Coast, and Oc. Engrg.*, ASCE, **126**(3), 144-152.

Wysession, M. E., E. A. Okal, and K. L. Miller, 1991: Intraplate seismicity of the Pacific basin, 1913-1988, *PAGEOPH*, **135**(2), 261-359.